AFRL-SR-BL-TR-98-

0149

REPORT DOCUMENTATION PAGE

Form Approved
OMB No. 0704-0188

Public reporting burden for this collection of information is estimated to average 1 hour per response, including the time for reviewing instructions, searching existing data sources, gathering and maintaining the data needed, and completing and reviewing the collection of information. Send comments regarding this burden estimate or any other aspect of this collection of information, including suggestions for reducing this burden, to Washington Headquarters Services, Directorate for Information Operations and Reports, 1215 Jefferson Davis Highway, Suite 1204, Arlington, VA 22202-4302, and to the Office of Management and Budget, Paperwork Reduction Project (0704-0188), Washington, DC 20503

1. AGENCY USE ONLY (Leave blank)	2. REPORT DATE 12/97	3. REPORT TYPE AND DATES COVERED Final 3/1/95 - 7/31/97

4. TITLE AND SUBTITLE Equipment for Neural Network Determination of Optical Phase Corrections Using Parallel Optical Hardware and Control Using Micromachined Microjets	5. FUNDING NUMBERS Contract/Grant Number F49620-95-1-0181

6. AUTHOR(S)
Mark Allen, Ari Glezer, Nan Marie Jokerst

7. PERFORMING ORGANIZATION NAME(S) AND ADDRESS(ES) Georgia Institute of Technology School of Electrical & Computer Engineering Atlanta, GA 30332 Drs. Nan Marie Jokerst, Mark Allen, Ari Glezer	8. PERFORMING ORGANIZATION REPORT NUMBER

9. SPONSORING/MONITORING AGENCY NAME(S) AND ADDRESS(ES) Air Force Office of Scientific Research NA	10. SPONSORING/MONITORING AGENCY REPORT NUMBER

11. SUPPLEMENTARY NOTES COR:
Dr. James McMichael

12a. DISTRIBUTION/AVAILABILITY STATEMENT unlimited	12b. DISTRIBUTION CODE

13. ABSTRACT (Maximum 200 words)

Herein, we report upon the purchase of equipment used for the development of diagnostic and manipulation hardware associated with the aero-optic effect. First, we report upon the purchase of diagnostic equipment associated with the measurement of turbulent flows. Second, we report upon the purchase of semiconductor etching hardware used in the hardware implementation of a diagnostic high frame rate "smart" camera for imaging turbulent flows and for the realization of bulk micromachined microjets to influence turbulent flows.

DTIC QUALITY INSPECTED 4

14. SUBJECT TERMS Aero-optics microjets smart imaging laser fluorescence	15. NUMBER OF PAGES 24
	16. PRICE CODE

17. SECURITY CLASSIFICATION OF REPORT unclassified	18. SECURITY CLASSIFICATION OF THIS PAGE unclassified	19. SECURITY CLASSIFICATION OF ABSTRACT unclassified	20. LIMITATION OF ABSTRACT unlimited

NSN 7540-01-280-5500

Standard Form 298 (Rev. 2-89)
Prescribed by ANSI Std Z39-18 298-102

Equipment for Neural Network Determination of Optical Phase Corrections Using Parallel Optical Hardware and Control Using Micromachined Microjets

Mark Allen, Ari Glezer*, Nan Marie Jokerst
School of Electrical and Computer Engineering
*School of Mechanical Engineering
Georgia Institute of Technology
Atlanta, GA   30332-0250

Final Report

Equipment for Neural Network Determination of Optical Phase Corrections Using Parallel Optical Hardware and Control Using Micromachined Microjets

Mark Allen, Ari Glezer, Nan Marie Jokerst

Georgia Institute of Technology

I. Introduction

Herein, we report upon the purchase of equipment used for the development of diagnostic and manipulation hardware associated with the aero-optic effect. First, we report upon the purchase of diagnostic equipment associated with the measurement of turbulent flows. Second, we report upon the purchase of semiconductor etching hardware used in the hardware implementation of a diagnostic high frame rate "smart" camera for imaging turbulent flows and for the realization of bulk micromachined microjets to influence turbulent flows.

II. Equipment Purchased

The following equipment was purchased under this DURIP Grant:

a. Equipment for Laser Induced Fluorescence Diagnostics

The equipment requested in the proposal for laser induced fluorescence diagnostics was a 20 W argon-ion laser. At the early stages of the work, we have developed a new, two-dye laser induced fluorescence diagnostic technique that has enabled us to obtain *simultaneous* cross-stream maps of aero optics effects *and* corrected distributions of the index of refraction. This substantial improvement in diagnostic capabilities mandated some changes in the equipment that was originally requested. In this process we were also able to take advantage of new hardware that did not exist at the time that the proposal was submitted.

1. **Innova 5W Argon Ion Laser** (Laser Innovations, $12,450). This CW laser is used for 2-color fluorescence measurements in our water shear layer facility. The laser is operated in a multi-line mode and is capable of delivering approx 2 W at 488 nm and 1.5 W at 514 nm.

2. **Two Dalsa CCD Digital Cameras** (Dalsa Inc, $5,154). These 128 x 128, 880 frames per second digital cameras are used for simultaneous acquisition of laser-induced fluorescence images in the cross stream plane of our water shear layer facility.

3. **Two Bitflow Digital Interface** (Bitflow Inc., $8,446). A high-speed computer interface board for the Dalsa cameras.

4. **ND YAG Laser** (Continuum, $47,840). A fast, double pulse YAG laser capable of 250 mJ/pulse as close as 5 ?sec apart. The laser will be used for simultaneous fluorescence and particle velocimetry measurements.

5. **PIV Diagnostics Software** (TSI Inc., $5,409). Software to be used in for particle image velocimetry along with the YAG laser.

6. **Two Macintosh Power PC Computers** (Apple Inc., $5,965). Fluorescence image processing and POD calculations

7. **Philips 100 Mhz Oscilloscope** (Fluke Inc., $2,069). Monitoring hardware for fluorescence experiments.

8. **Kron-Hite 2 Mhz Filter** ($472). Signal conditioning.

The use of this equipment is described in detail in Section IIIa.

b. Inductive Coupled Plasma Source for Polymer and Si Bosch Process Etching

An Inductively Coupled Plasma (ICP) system from Plasmatherm, Inc., has been purchased with contract funds. This ICP system is superior to an RIE, and enables fast, highly reproducible polymer etching, and, unlike an RIE, also enables deep Si trench etching for micromaching. Both of these processes and their systems applications are described in Section III. In the funded contract, the Air Force funding was $200,000, with matching of $41,000 from Georgia Tech. Of this $241,000 total, $160,000 was designated for use by the ICP etching system. The desired two chamber (one for polymers, one for Si etching, to maintain optimal cleanliness and repeatability) system cost was $849,600 from Plasma Therm, Inc.. A similar quote resulted from STS, Inc.. Due to the placement of other Plasma Therm systems at Georgia Tech, Plasma Therm was very interested in maintaining a high profile at Georgia Tech, and offered to Georgia Tech a Strategic Credit of $409,000, thus reducing the cost to $440,000. Additional addendum items raised the final cost to $451,200. *In addition to the $41,000 matching originally promised by Georgia Tech, Georgia Tech matched an additional (astonishing) $291,000 to acquire this sytem.* These negotiations were time-consuming, however, they ultimately resulted in a very high performance system.

The ICP uses a high density plasma discharge generated by applying rf power into an inductive coil capable of transmitting power into a low pressure gas. The coupling mechanism differs from that in a standard diode type reactive ion etching system in that the

power is magnetically applied and not directly applied through an electric field. Electrons are heated by an H field, which is the electric field that exists at right angles to the induced magnetic field. High plasma density can be achieved because power can be transferred into the bulk plasma via the magnetic field resultant from inductive coupling. This differs from capacitive coupling, where the allied electric field is attenuated by Debye shielding above the pre-sheath, and therefore, does not exist within the full plasma. Inductive coupled plasma sources have potential advantages over other high-density sources, such as ECR and Helicons, which include simplicity of concept, less stringent requirements on operating pressure, no requirement for magnetic fields, and rf power supplied at lower frequencies than microwave systems.

High density plasma sources, such as the ICP purchased herein, provide some advantages over conventional parallel plate plasma systems. In conventional RIE, the plasma density is limited by the method of coupling rf energy into the plasma. This limits the rates at which certain materials can be etched or deposited. This problem becomes particularly acute at reduced pressure where, with the efficiency of an IRE, the plasma density can become prohibitively low. Additionally, in RIE, the relationship between power and bias voltage is fixed at any given pressure and gas mixture. This limits bias sensitive applications to low power levels and renders some processing goals unachievable. High density plasma sources allow the bias voltage to be controlled independent of the total input power. Using this method, the process can be modified for independent control over ion current and bias voltage. This is possible because the primary plasma source does not, by itself, generate a power dependent bias voltage on the substrate. Bias voltage is controlled through the use of a second rf power supply used exclusively to generate the substrate bias voltage. In this method, the ion current density and plasma density is controlled by the power level applied to the high density source and the substrate bias is controlled by the power level applied by the power supply used for substrate bias. Thus, higher etch rates, good reproducibility, and a high degree of surface uniformity can be achieved with ICP systems.

III. Utility of Equipment Purchased for Flow Diagnostics and Control

a. Use of the Equipment for Laser Induced Fluorescence Diagnostics

The requested equipment has been critical for our work on used for neural network determination of optical phase correction in a plane shear layer that has been separately funded by AFOSR (Grants F49620-95-1-0246 and F49620-95-1-0297).

Neural networks that allow aero-optic phase correction to be made using localized measurements without an external probe beam are being developed in an information-rich laboratory environment. The neural networks are trained to relate phase corrections to low-order modal descriptions of a plane shear layer obtained by a proper orthogonal decomposition (POD) applied to index of refraction data. Optical measurements are taken in a plane shear layer between two uniform streams with different temperatures. The training sequence will use actuators to influence the flow, thus providing the networks with a broader operational range. Elements critical to the training include development of a three-dimensionally interconnected high frame rate optoelectronic smart camera, extraction of the velocity field using two scalars, and determination of modal coefficients in a low-order description of the flow. The ultimate objective is to simultaneously determine the three-dimensional index of refraction field and the resulting optical phase front distortion in the plane shear layer, thereby providing real-time correlation between index variation and optical phase shift to the neural networks.
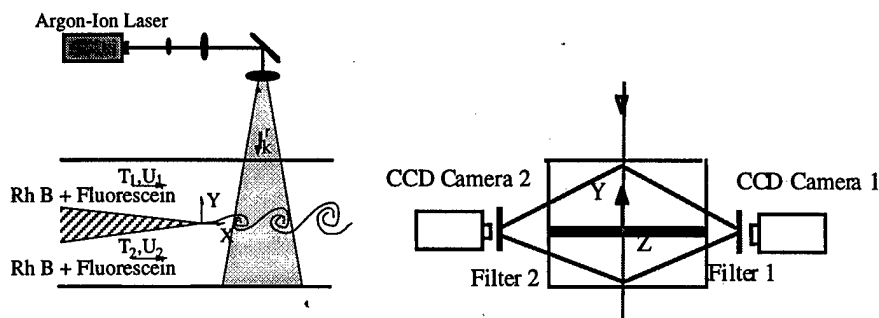
III.a.1. Global Measurements of Optical Distortion in a Plane Shear Layer

III.a.1.1 Experimental Setup

Optical distortion of a sheet of light transmitted through the cross-stream plane of a 2-D shear layer between two streams with unequal temperatures (Figure 1) is investigated in a closed-return water channel. The use of temperature as a thermal analog to mixing of two species has the distinct advantage that temperature mixes in water with a Prandtl number of about seven, which is much closer to the Prandtl number for mixing of temperature (and hence index of refraction variations) in gases (about unity) than is the Schmidt number for mixing of concentration in water (on the order of 1000 for typical organic dyes).

The water in the facility is uniformly mixed with two fluorescent dyes: Rohdamine B and disodium Fluorescein which are simultaneously excited in planar cross sections of the

flow using a multi-line argon Ion laser as shown schematically in Figure 1. The concentration of each of the dyes is selected to optimize the fluorescence intensity and minimize the attenuation of the transmitted light. Instantaneous temperature distributions (from which the index of refraction field and the degree of mixedness can be directly determined) are obtained with resolution of $0.05^{\circ}C$ using the temperature-dependent fluorescence of Rhodamine B which has maximum emission at 585 nm with fluorescence quantum yield of 0.4 between $10^{\circ}C$ and $30^{\circ}C$.

Argon-Ion Laser

T_1, U_1
Rh B + Fluorescein

T_2, U_2
Rh B + Fluorescein

CCD Camera 2   CCD Camera 1

Filter 2   Filter 1

Figure 1

The temperature dependence of the luminescence is tested in a separate isothermal calibration cell and is linearly proportional to the temperature of the dye solution with a temperature coefficient of 2.1%/K. Thermal equilibration occurs on the very fast time scale of the translational/vibrational equilibration (typically much less than ten nanoseconds). Because the fluorescence images of Rhodamine B are modified by aero-optical effects, a correction scheme is applied in order to recover the *actual* distributions of temperature and index of refraction using. This is accomplished using fluorescence images of both Rhodamine B (maximum emission at 585 nm) and disodium Fluorescein (maximum emission at 510 nm) the fluorescence of which is weakly dependent on temperature. The images are captured *simultaneously* with two imaging systems and separated using optical filters. Simultaneous images of the intensity distributions are measured using two high-speed (128 x 128, 800 fps) CCD cameras having independently controlled gain and offset. Each camera is driven by a PCI board with variable scan input from a host laboratory computer. The attenuation along the transmitted light sheet in each frame is corrected using a reference image that is acquired when the temperatures of two streams are identical.

At present, we are also developing an imaging technique that will enable us to obtain concurrent velocity and fluorescence measurements in the field of view using a double-

pulsed YAG laser and particle image velocimetry based on uniform seeding of 40 μm particles in both streams of the shear layer facility. We anticipate that the velocity measurements will enhance the training performance of the neural networks by providing predictive capabilities.

III.a.1.2. Aero-Optical Effects

A digitized image (taken at 220 fps) showing of the temperature distribution in the cross-stream plane is shown in Figure 2a. The streamwise domain begins at x=10 cm (the wavelength of the fundamental K-H instability is approximately 4 cm), the field of view is 4.5 cm in the streamwise and cross-stream directions, the Reynolds number based on the vorticity thickness is 1600, the free stream velocities are 24 and 8 cm/s, and the corresponding free-stream temperatures are 20 and 25°C. The laser sheet propagates from top (cold stream) to bottom and high intensity regions correspond to low temperatures (the fluorescence intensity decreases linearly with the temperature). This streamwise domain is upstream from the onset of (natural) mixing transition and there is a sharp interface between the two streams. The spatial resolution (approximately 300 μm) is of the same order as temperature diffusion scales. The instantaneous and time-averaged cross-stream temperature distributions at x=13 cm are shown in Figures 2b and c and indicate uniform temperature distributions within the free streams and a sharp changes at the interface.

An important feature of the optical transmission through the layer is the appearance of cross-stream pairs of high- and low-intensity streaks in images of the fluorescence intensity. The streaks originate from regions of the flow where the angle between the local gradients of the index of refraction and the wave vector of the incident light is large and are advected with the vortex. Figure 2d shows a view of the spanwise vortex and the accompanying streaks when the mean temperature is removed (two rays are traced on top of the image). A given ray within the sheet is refracted at a cumulative angle θ that depends on the local index of refraction gradients in its path.
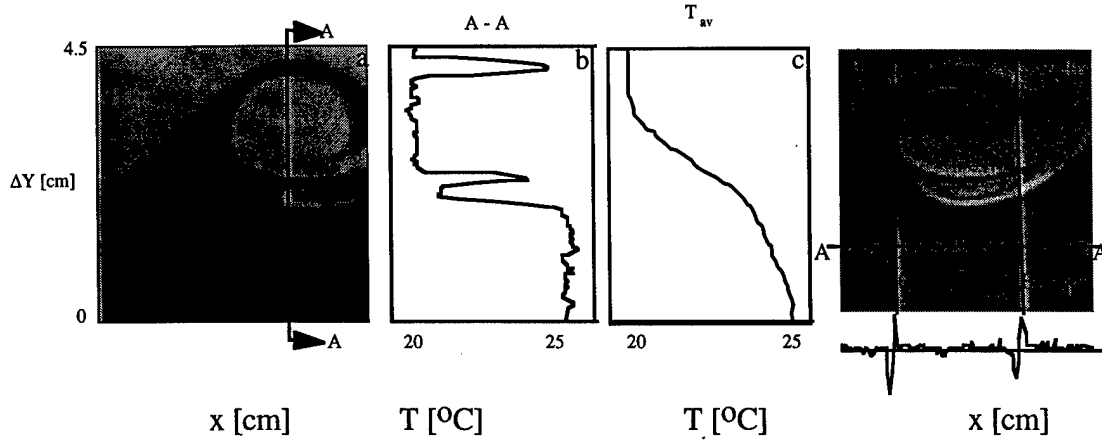
A - A

T_{av}

Figure 2

The streak pair on the right appears to form as a result of total reflection at the interface where the critical angle of incidence for which the angle of refraction is 90° is 88.5^o. For angles of incidence larger than the critical angle, some rays experience total reflection, and, as a result, a pair of adjacent low- and high-intensity streaks are formed as demonstrated by the streamwise trace of the intensity distribution that is plotted below the frame. At the interface on the left, total internal reflection is not possible because the rays propagate from the hot stream into the cold stream and thus $n_2 > n_1$. The formation of a low-intensity streak at this interface is due to the fact that rays at large angles of incidence with respect to the interface refract at larger angles. As the angle of incidence approaches 90° the refraction effect becomes significant enough to cause formation of the low- and high-intensity streaks that are comparable to the streaks formed by total reflection.

Because the fluorescence of disodium Fluorescein is only weakly dependent on temperature, its fluorescence images are primarily affected by the aero optics effects. These images are captured simultaneously with the fluorescence images of Rhodamine B and are used to correct the aero optical effects and recover the actual temperature distributions $T(x,y)$:

$$T(x,y) = f_{calib}\{[I_T(x,y) - I_{T\,ref}(x,y)] - c_f[I_i(x,y) - I_{i\,ref}(x,y)]\}$$

where $I_T(x,y)$ is the intensity of Rhodamine B, I_i is the intensity of disodium Fluorescein, c_f is a scaling constant and f_{calib} is the calibration function of the temperature dependence of Rhodamine B. The effectiveness of the correction procedure is tested at somewhat higher free stream velocities (39 and 13 cm/s) and the resulting intensity maps of

Rhodamine B and disodium Fluorescein are shown in Figure 3. The simultaneous intensity maps of Rhodamine B and disodium Fluorescein are shown in Figures 3a and b, respectively. The aero-optic corrected temperature map is shown in Figure 3c and demonstrates that the streaks pairs are substantially removed. Streamwise temperature distributions in the low-speed (hot) free stream with and without the correction are shown in Figure 3d. It is important to note that the correction procedure requires only the two simultaneous intensity maps, reference intensity maps for the isothermal flow conditions, and knowledge of the temperature sensitivity of the fluorescent dyes.

III.a.1.3. Manipulation of aero-optical effects using direct small scale excitation

The most prominent aero-optical effects within the plane shear layer are associated with the rollup and advection of the primary vortices. Specifically, pairs of high- and low-intensity streaks in intensity maps of the transmitted light are formed when the angle between the local index of refraction gradients and the wave vector of the incident light is large. The intensity variation within these streaks depends on the length scale and magnitude of the index of refraction gradients. Thus, it might be expected that aero-optical effects of the interface between the two streams can be mitigated by direct excitation of
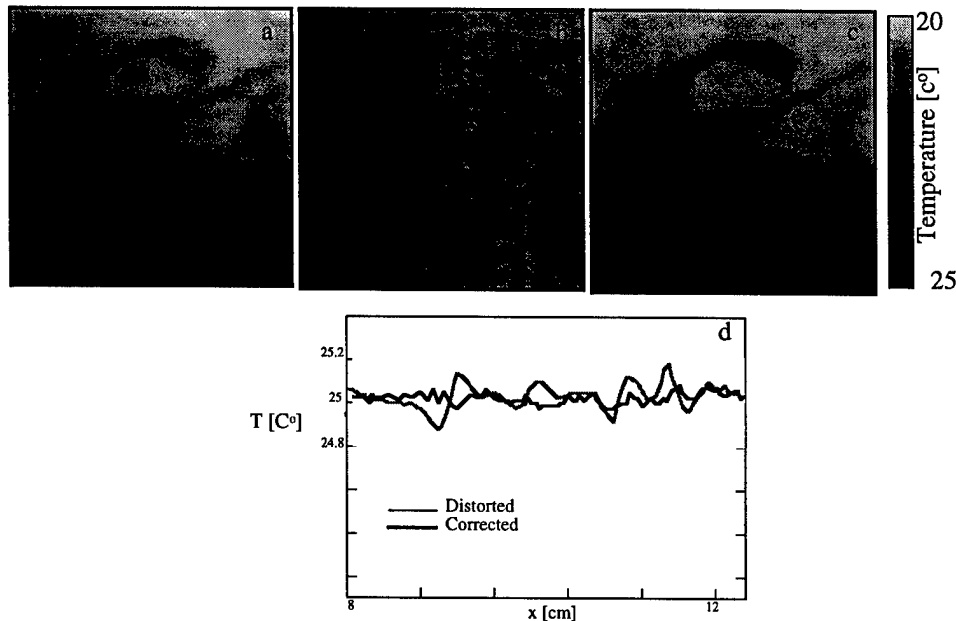

Figure 3

vortical structures within the dissipation range of the base flow having characteristic scales that are one to two orders of magnitude smaller than the wavelength of the primary (Kelvin-

Helmholtz) instability. In the present experiments, small-scale motions are forced using an array of piezoelectric actuator pairs (each 20 mm long and 8 mm wide) cantilevered at the trailing edge of the flow partition and operated at their nominal resonance frequency (225 Hz). The advantage of this actuation approach, which was developed by Wiltse and Glezer (1993) and later also applied by Jacobson (1995), is that the voltage induced strain in the piezoelectric material is substantially amplified and results in a significant tip deflection. Each actuator pair produces a zero mass flux jet that is synthesized from the surrounding fluid and is comprised of a train of small-scale vortex pairs.

The effect of direct small-scale excitation on the evolution of the streaks in the absence of the aero optics correction procedure is shown in Figure 4 (free stream velocities of 24 cm/s and 8 cm/s). The instantaneous intensity map for the unforced case is shown for reference in Figure 4a. The excitation leads to mixing enhancement by increasing the interface between the two streams and, as a result, the streaks in instantaneous intensity maps of the forced flow are significantly weaker than in the unforced flow. This is further demonstrated in Figure 4c which shows streamwise intensity distributions (measured 0.5 cm from the bottom of the frame) for the unforced and forced flow. Although it appears that the number of streaks (as represented by local extremae) increases when the flow is forced, their magnitude is significantly lower than for the unforced case.
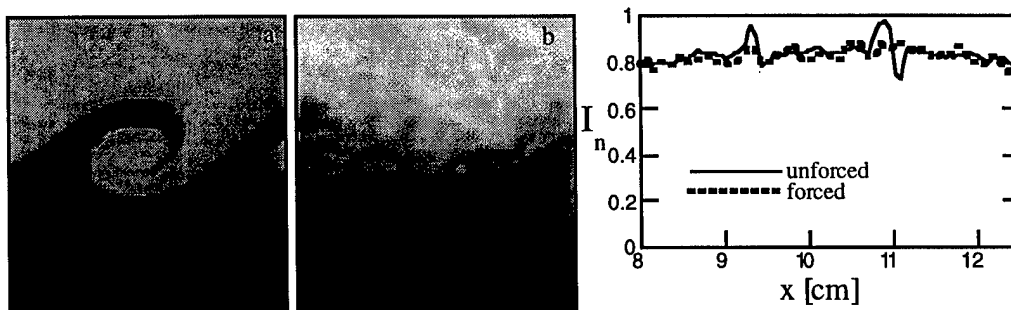

Figure 4

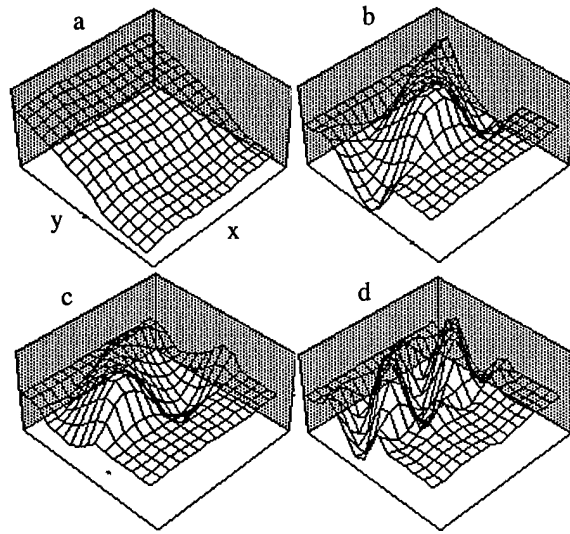### III.a.1.4   Proper Orthogonal Decomposition (POD)

One of the critical elements for real-time computation of optical phase distortion is the development of a low-order representation of volumetric index field using proper orthogonal decomposition (POD) of the temperature data, that will allow neural networks to be trained using orders of magnitude less data than if such representation was not available. Using experimental data for the cross-stream dependence of the streamwise velocity

component in a plane mixing layer, Glezer, Kadioglu & Pearlstein (1989) showed that a modification of Lumley's (1967, 1980) classical proper orthogonal decomposition leads to modes that efficiently capture a large fraction of the "action" in a periodically forced flow (for three-dimensional data the "action" is equivalent to kinetic energy.) The extended POD (EPOD) technique has an advantage over the usual POD (e.g., Aubry, Holmes, Lumley & Stone 1988) in that it avoids computation of the second-order correlations required by Lumley's (1967, 1980) approach. Instead, it concatenates data from an ensemble of records, each of duration τ_s sampled at a frequency f_s. The mode shapes $\varphi_i(x, y, z)$ determined by this procedure coincide with those obtained by the classical procedure in the limit of very long records. The general idea is to expand temperature data in a time series

$$T(x, y, z, t) = \sum_{i=1}^{N} a_i(t)\, \varphi_i(x, y, z) \tag{1}$$

obtained from successive frames of the CCD camera where $a_i(t)$ are time dependent expansion coefficients. To the extent that the modes differ from those of the classical procedure, the effect is to make them somewhat suboptimal, in the sense that a given number N of them capture less of the "action" in the scalar field than would N modes computed from long time series. The advantage is that calculation of the modes requires shorter data records, and is hence better suited for the present application, in which storage and computation of second-order correlations for fully three-dimensional data is likely to be computationally burdensome.

Figure 5 (a-d) shows the spanwise structure of the four most energetic proper orthogonal modes of the temperature field of the unforced mixing layer using 1200 successive frames. Modes m = 1, 2 and 3 (not counting the mode m = 0 corresponding to the mean flow) contain about 25%, 24 % and 8% of the kinetic energy in the flow. The most energetic mode (m = 1) corresponds to the large vortical structures in the unforced flow, and the other modes correspond to smaller scales. For the present data, the first 30 two-dimensional eigenvectors capture more than 90% of the total energy of the temperature field. These modes are than used to reconstruct the instantaneous temperature (intensity) field, and the time coefficients in the series expansion are computed using a least-square fit.

Figure 5

The applicability of the proper orthogonal decomposition technique for the analysis of turbulent flows is further tested when the flow is periodically forced (for the same flow conditions). Excitation of spanwise instability modes at high frequency was accomplished by a spanwise array of a planar bimorph actuators driven with an amplitude modulated excitation waveform where the carrier frequency is 85 Hz and the modulating frequency is 3 Hz. Figure 6 shows a sequence of four successive images of the forced flow on the top row. The reconstructed images (using 90 modes) are shown on the bottom row and demonstrate that the EPOD procedure can effectively capture the small-scale features that
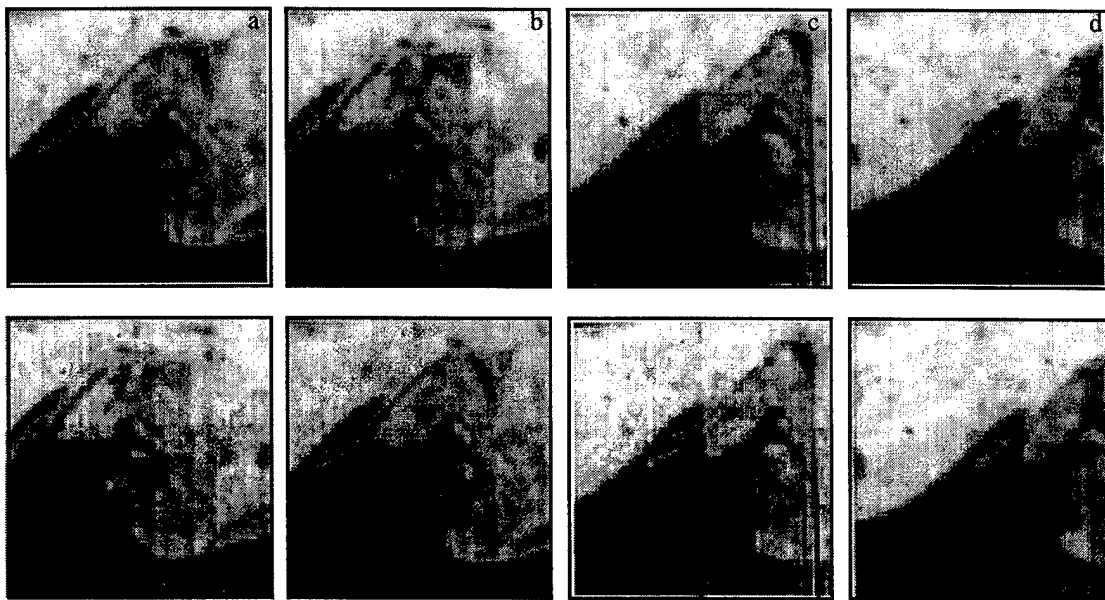
Figure 6

are introduced by the forcing and the aero optics effects. The relative error between the original and the reconstructed images is less than 1% when 90 eigenmodes are used in the reconstruction. Because only 90 coefficients are necessary to describe the flow once the modes are known, the complexity of the description of flow dynamics is effectively reduced by two orders of magnitude. The quality of the reconstructed image and the relative error between the original and the reconstructed images are directly proportional to the number of modes that are used in the reconstruction.

III.a.2. Extraction of Solenoidal Velocity Fields from Scalar Data

Earlier, we developed a concept for determining n-dimensional ($n=2,3$) solenoidal velocity fields from measurement of n-1 passive or reactive scalars (Pearlstein & Carpenter, 1995). The approach uses the continuity equation (which is linear in, and involves first derivatives of, u, v, and w), and n-1 scalar transport equations, each linear in u, v, and w. These n equations are rewritten as a system of linear, first-order, <u>uncoupled</u> hyperbolic equations for the n velocity components, which can be determined by integration along characteristics.

Last year, we completed a computational proof-of-concept study (Carpenter & Pearlstein 1996) in which the concept is reduced to an algorithm and applied to a steady, two-dimensional, diverging channel flow, chosen because it diverges downstream, like a plane shear layer.

We have now parallelized this algorithm, initially on a 224-processor SGI Origin 2000 machine. The approach takes advantage of the fact that, at each time step, the equations along a given characteristic are uncoupled from the equations along every other characteristic, thus allowing the computational load to be efficiently distributed among the processors. (This decoupling is distinct from the decoupling of the equations for each velocity component from those for the other components *on the same characteristic*. As expected, the speedups are essentially linear in the number of processors ($T = a + b/N$, where T is the running time, and N is the number of processors).

III.a.3. Development of Low-Dimensional Models of Aero-Optic Flows

Our work in this area focuses on two problems central to development of low-order models of complex flows: representation of velocity and temperature fields in terms of a

small number of basis functions, and development of dynamical models (in terms of ordinary differential equations) governing the evolution of modal coefficients.

III.a.3.1 Efficient Computation of Two- and Three-Dimensional Modal Decompositions

Measurements at Georgia Tech provide two-dimensional slices of the temperature field, obtained using a water-soluble dye whose fluorescence quantum yield is a sensitive function of temperature. By expanding the temperature field using a set of basis functions, we can write the temperature field in the form of (1), where the modes $\varphi_i(x, y, z)$ are obtained using the extended proper orthogonal decomposition technique described by Glezer, Kadioglu, and Pearlstein (1989).

The spatial modes recovered at Georgia Tech and Illinois from a large ensemble of two-dimensional images of temperature in the shear layer revealed that modes 5 and 6 contain considerably more fine-scale structure than either the preceding modes or the following modes. This result was contrary to what we expected on the basis of previous results for one-dimensional modes, in which the amount of fine-scale structure increases monotonically with mode number. Careful processing of temperature data from Georgia Tech has since revealed an A/D conversion error traceable to nonlinear hardware performance at high data rates. This error has now been corrected, and processing of correctly-digitized data will resume shortly.

III.a.3.2. Development of Low-Dimensional Dynamical Models

A set of ordinary differential equations can be generated from a modal decomposition such as (1) by projecting the governing equations (Navier-Stokes and conservation of energy in this case) onto the modal representation, leading to a system of ordinary differential equations (ODEs) of the form

$$\frac{db_i}{dt} = f_i(b_1, b_2, ..., b_N) \ . \tag{2}$$

Since the nonlinearities in the governing equations (i.e., the nonlinear inertial term and the $\mathbf{v} \cdot \nabla T$ t term in the energy equation) are quadratic, the resulting ODE system will be of the form

$$\frac{db_i}{dt} = \sum_{j=1}^{N} q_{ij} b_j + \sum_{j=1}^{N} \sum_{k=1}^{N} r_{ijk} b_j b_k + g_i(t) \ , \tag{3}$$

where the final terms will be constants absent time-dependent forcing.

Since the data initially available are two-dimensional temperature fields, it is not possible to compute three-dimensional modes, or to project the Navier-Stokes equations. Instead, we take a more empirical approach, and seek to use the two-dimensional temperature fields to obtain a differential equation system governing (approximately) the evolution of the temperature field, absent direct information about the velocity field.

Thus, we treat the problem of determining the coefficients in (3) as a *linear* parameter identification problem. Given the modes as discussed in the previous section, we first determine the temporal coefficients $b_i(t)$ by a standard "reconstruction" at each time. This in turn allows the coefficients in (3) to be determined by a noniterative, *linear* least squares procedure, using numerical estimates of the $b_i(t)$ and their first derivatives. This will provide a system of dynamical equations for evolution of two-dimensional "slices" of the temperature field, without directly dealing with the underlying velocity field and three-dimensionality.

We are also pursuing an approach in which coefficients of the velocity field are treated as unknown dynamical variables (among the $b_i(t)$). In that case, only some dynamical variables in (3) are known (the temperature coefficients). We have developed a technique to eliminate the velocity coefficients, leaving a lower-order ODE system for the coefficients of the temperature modes. Using time series for these, we finally get a *nonlinear* polynomial system in the coefficients g_i, q_{ij}, and r_{ijk}. Using the Brouwer fixed point theorem and a variant of Krawczyk's mapping, we have developed an algorithm and code to find all real solutions of that system (Cotrell & Pearlstein, submitted for publication).

The algorithm systematically examines regions in R^N and decides whether a) there is a unique solution, in which case the solution is rapidly isolated; b) there is no solution, in which case no further consideration of the region is required; or c) neither of the above conclusions is possible, in which case the region is bisected, and the same process is applied to the two smaller regions. Parallelization is easily achieved in this algorithm, since

regions can be assigned to available processors completely independently. When a region has been examined (with disposition a, b, or c), the processor then becomes available for the next region. Since nearly the entire computational burden resides in the examination of the regions, nearly linear speedup can be expected.

We have parallelized the nonlinear equation solver for MIMD (multiple instruction, multiple data) architectures, and are currently running it on an SGI Origin 2000 machine. Nearly linearly speedup has been achieved for large systems of quadratically nonlinear equations.

To better understand the issues that will be important in developing real-time implementations of this algorithm, we are currently rewriting the code for SIMD (single instruction, multiple data) architectures, using the MPI programming model, and have requested access to the 256-processor IBM SP SIMD machine at the Major Shared Resource Center (ASC, WPAFB), to test and run the code.

### b. Etching of Polymers for Hybrid Integration of Smart Fast Camera Hardware

To enable diagnostic measurement on turbulent flows, an imaging system must have the highest frame rate possible to resolve the maximum detail at the desired flow rates. To achieve this type of frame rate, signal processing, such as pre-processing and compression, on the focal plane is critical, since limited quantities of image data can be transferred off the focal plane at high rates. Thus, we are constructing high frame rate, "smart" (i.e., processing on the focal plane) cameras for flow diagnostics. The real-time utilization of image sequences at high frame rates can be achieved with an optically interconnected massively parallel processor. A focal plane processing chip with an on-chip array of sigma delta analog to digital converter front ends under each pixel is under construction. This two layer chip is a scaleable high frame rate image capture building block, which uses a third layer of data processing to filter the sigma delta front end data to obtain images. The use of an array of vertically optically connected processors beneath the imaging array chip is an effective solution to this challenging data processing task.

To achieve image processing systems that operate in real time, on large images with frame rates in the high kHz or MHz is beyond the capability of today's imaging systems. For example, a sigma delta analog to digital converter (ADC) generating a sequence of 256x256 8 bit images at a frame rate of 400 kHz must be clocked at more than 1.8 THz. Even when parallel ADCs are placed along the edge of the imaging array, the problem is

only partially mitigated because the speed at which the ADCs must operate still increases with image size. To generate 256x256 8 bit images at a frame rate of 400 kHz, 256 ADCs need to be clocked at more than 7.3 GHz.

Herein, we describe a chip that implements a fully parallel front end with one ADC per pixel. This provides a scaleable solution to the real time high frame rate image capture problem when it is coupled to a massively parallel optically interconnected processor. We show that to generate a sequence of 256x256, 8 bit images at a frame rate of 400 kHz, a 32x32 array of 230 MHz pipelined processors (each operating at 950 MIPS) is required. To keep the design scaleable the processors must reside beneath the imaging chip, which uses 3-D electrical interconnect for parallel connection to the detector plane. To connect to subsequent layers of processing, a through-substrate parallel optical data link is used.

To overcome the limitations of serial and semi-parallel readout, we have implemented a focal plane array (FPA) using a fully parallel readout architecture. Figure 7 shows this architecture, in which each pixel has its own ADC. To minimize the area of the ADC circuitry, only the front end of the sigma delta converter is implemented per pixel. Since sigma delta converters process only digital data after the front end, further noise cannot be introduced to the signal by shifting the now digital data. A processor is then needed to complete the ADC process. By grouping the pixels into subarrays, each can be served by one processing unit to perform the conversion. To provide the high data rate necessary between the imaging array/ADCs and processor, an integrated optoelectronic emitter on each subarray enables vertical optical through-silicon output of digital image data from the focal plane to the processor stacked below each subarray. This vertical coupling to the image plane allows the detector and processor arrays to be scaled while maintaining a fixed level of processing per pixel. The number of pixels included in the subarray is dependent on the bandwidth of the processor circuits. The SIMPil processor [H. Cat., J. Eble, D. Wills, V. De, M. Brooke, N. Jokerst] is being implemented for this program. If an 8x8 subarray is used, the size of the processor and focal plane subarray match well, so by tiling an 8x8 array of processor chips each containing 16 nodes, a 256x256 pixel resolution focal plane can be achieved.

Detector and ADC layer

Through wafer
optoelectronic
communication

SIMPil processor layer
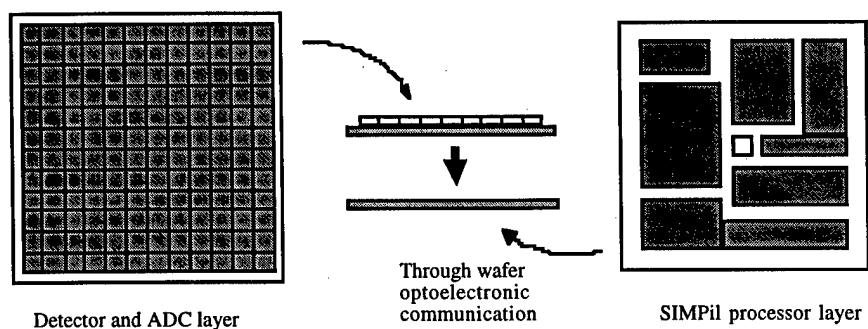
Figure 7. Parallel on-focal-plane ADC with vertical optical link to SIMPil processor

Figure 8 is a photomicrograph of a fabricated chip with an 8×8 array of ADCs, associated readout shift registers, and emitter driver. This chip sits above the SIMPil processor, shown in Figure 9.
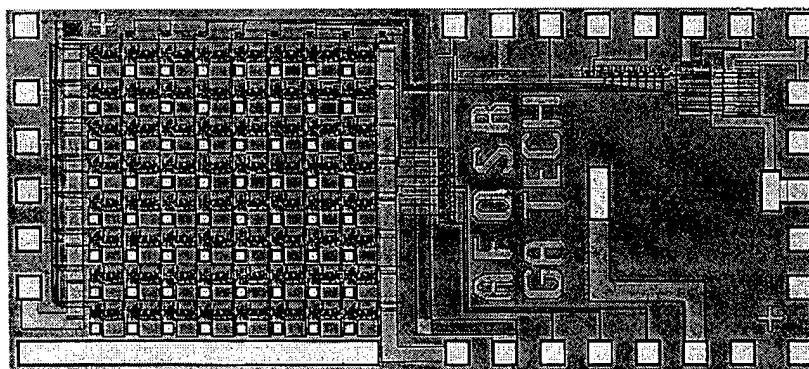
**Figure 8. Si chip with 8 × 8 ADCs, shift registers, and emitter driver.**
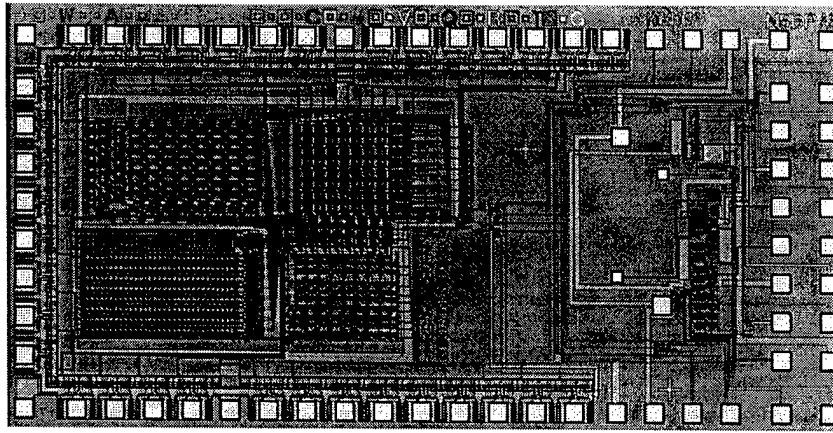
Figure 9. Photomicrograph of the SIMPil node and receiver amplifier.

To integrate the detector imaging array onto the silicon circuitry, and the emitter and detector for the through-Si vertical optical link, hybrid integration has been used. Hybrid integration, or the bonding of separately grown compound semiconductor devices on top of silicon circuitry, is an attractive option for the integration of the detector array and the through-substrate emitter and detector devices [C. Camperi-Ginestet, Y.W. Kim, N.M. Jokerst, M.G. Allen, M.A. Brooke]. The optoelectronic materials are fabricated separately from the electronics, and multiple types of materials and devices can be integrated onto the same circuit. Thus, for the imaging array, GaAs-based detectors have been integrated onto the Si ADCs, and InP-based devices were bonded to the through-Si emitter and detector sites (these devices operate at wavelengths to which the Si is transparent). Figure 10a is a photomicrograph of an unbonded Si circuit as received from the MOSIS foundry. Figure 10b is a photomicrograph of the GaAs thin film detector array bonded onto the top of the circuitry, and Figure 10c shows the final integrated optoelectronic circuit, with the common top contact deposited onto the detector array, connecting the array to the silicon circuit. Each detector is individually interconnected to the silicon circuitry which lies beneath it through a metallized overglass cut on the circuit.
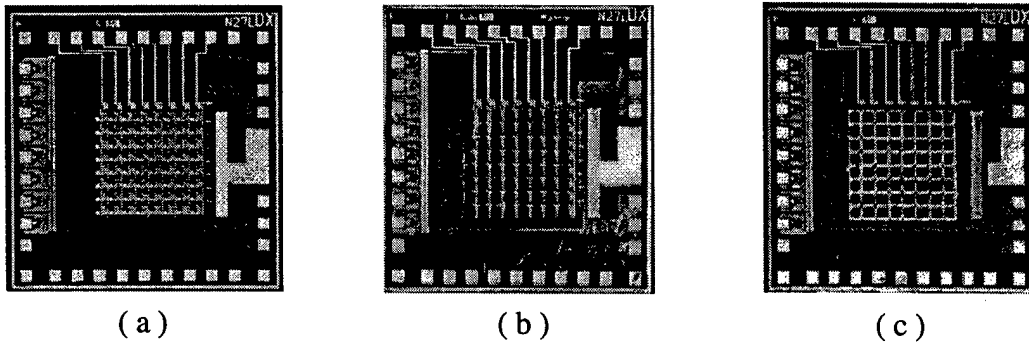
Figure 10. Photomicrographs: (a) the unintegrated Si circuit; (b) the Si circuit with a bonded thin-film array; (c) the integrated array with a common top contact.

Critical to the implementation of this system is the semiconductor processing to construct the three dimensional interconnection. Both the through-Si optoelectronic link (at a wavelength to which the Si is transparent) and the detector array on top of the ADCs must be integrated. In both cases, first, the circuits must be planarized prior to compound semiconductor thin film device integration. Second, the top and bottom contacts to the thin film devices must be electrically isolated. In both cases, planarizing, insulating polyimide (duPont PI 2611, a standard microelectronics material) is used, and vias in this polyimide must be formed to realize contact to the circuits or device. The etcher that has been purchased with the equipment funds is used to etch these vias in the polyimide.

The process for both of these integration steps is critical to the yield and manufacturability of the polyimide process, and hence, the camera hardware implementation. To prepare the silicon circuit for the bonding of the imaging arrays, the foundry Si CMOS VLSI circuit is mounted on a glass slide using duPont polyimide for handling. After a soft bake at 120°F, the circuit is then spin coated with a layer of polyimide followed by another soft bake and cure cycle. Each layer of polyimide has a thickness of approximately 3 μm. It is then necessary to open vias in the polyimide to enable electrical connection of the array pixels to the circuitry. To accomplish this, an aluminum (Al) mask was deposited on the polyimide-coated circuit using a thermal evaporator, and windows were defined in the Al at the locations of the bottom contact pads on the circuit. Contact pads and via holes are typically 25 μm on a side squares. The polyimide uncovered by the removal of the Al was etched away using a reactive ion etch

(RIE) system, which is the utility of the new ICP system. The recipe for etching polyimide consists of 5 parts CHF_3 mixed with 45 parts O_2 at a pressure of 300 mtorr, a power of 300 W, and a time of 10 minutes. The new ICP system will reduce this time by a factor of 10, and will provide a higher degree of repeatability and unformity for higher yield and larger area processing.

Once the polyimide windows are completely etched, the Al mask is removed using a heated potassium cyanate wet chemical etch, and the 250 μm square gold pads which were bonded to the ohmic contact pads on the detector were deposited. To insure good electrical connection from the circuit up over the polyimide, the Ti/Au contact layers were deposited using a DC sputtering system. It was used in lieu of an e-beam or filament evaporator because it has a less directional deposition, which will decrease the probability of an open between the circuit and the pads on the polyimide. Once these pads were defined, the detector array is bonded to the circuit.

The next steps were the spin coating of polyimide (for contact isolation) and a polyimide cure, and the circuit with the integrated detector array are ready for via cuts for the array top contact. Windows in the polyimide are etched using RIE (again, the ICP purchased under this funding is best for this purpose) to access the circuit pads for the top contact of the array in the same manner as the initial polyimide cuts using the $CHF_3:O_2$ recipe. The individual top contacts for each pixel are defined using standard negative photolithographic processes and the top ohmic contacts are deposited using a thermal evaporator. The contact consisted of a rectangle that covered the pixel and the polyimide via to the circuit with a typically 100 μm window centered over the detector to allow incident light. After the ohmic evaporation is complete using the thermal evaporator, the circuit is placed in the DC sputtering system where an additional 2000 A gold layer is deposited. This, like the first metal deposition done on the circuit for the Ti/Au pads, decreases the probability of an electrical open between the top of the device and the circuit. This completed the integration steps for the detector array.

c. MEMS-based Microjets and ICP Modification

We have developed an approach to the manipulation and control of shear flows using novel fluidic technology based on synthetic jets. These jets have the property of being *zero-mass-flux* in nature; i.e., they are synthesized from the working fluid in the flow system in which they are embedded. Although there is no net mass injection into the

overall system, the jets allow momentum transfer into the embedding flow. The interaction of synthetic jets and an embedding flow near the flow boundary leads to the formation of closed recirculation regions and thus an *apparent* modification of the flow boundary. *These features enable synthetic jets to effect significant global modifications in embedding flows on scales that are one to two orders of magnitude larger than the characteristic length scale of the jets themselves.* These capabilities have been demonstrated in a series of pilot investigations including thrust vectoring and modification of aerodynamic surfaces.

Conventional methods for the modification of lift and drag on aerodynamic surfaces have primarily focused on delay of separation or inducement of reattachment by introducing small disturbances into the upstream wall boundary layer. These methods have been used with varying degrees of success and depend on the receptivity of the boundary layer to excitation within a relatively narrow bandwidth. Because synthetic jets operate with no net mass flux, a unique feature of their interaction with an embedding flow near a solid surface is that they can effectively modify the *apparent aerodynamic shape* of the surface because they engender the formation of closed streamline flow regimes near the surfaces. Thus, the aerodynamic characteristics (i.e., lift and drag) of an airfoil which are critically dependent on the location of its front and rear stagnation points and on its camber and thickness can be altered by synthetic jet actuators without the use of movable flaps.

Recently, synthetic jets based on MEMS technology have been realized at Georgia Tech, using standard silicon-based micromachining techniques (Coe, Allen, Glezer et. al., 1995). A cross-section of a typical microjet in shown in Figure 11. In this design, the orifice and actuator are incorporated into the same wafer. Although only a single jet is shown in this configuration, extension of this concept to addressable arrays of microjets is straightforward and has been realized by us.

Synthetic jets are formed by an actuator comprising an orifice hole, an underlying actuator cavity, and a movable membrane bounding one of the cavity surfaces. These jets operate without net mass injection across the actuator surface and are thus comprised entirely of entrained surrounding fluid and are in effect synthesized by a train of vortices. Each vortex is formed at the edge of the orifice, and is driven by the motion of a diaphragm at the bottom of a sealed shallow cavity under the orifice plate. The vortices, and thus the characteristic dimensions of the jets, scale with the characteristic dimension of the orifices. Because the motion of the diaphragm is extremely small and it can be driven at resonance (e.g., by a piezoelectric actuator), the electrical power input to the actuator is typically small (in recent experiments at Georgia Tech, a millimeter-scale synthetic jet actuator was used for thrust vectoring of primary jets that are at least two orders of magnitude larger). In the experiments reported here, the diaphragm is driven at 1.3 kHz.
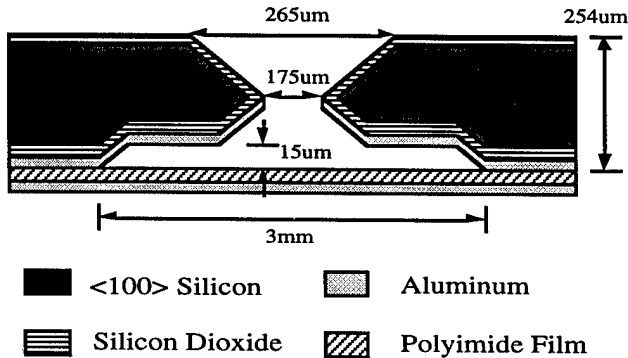
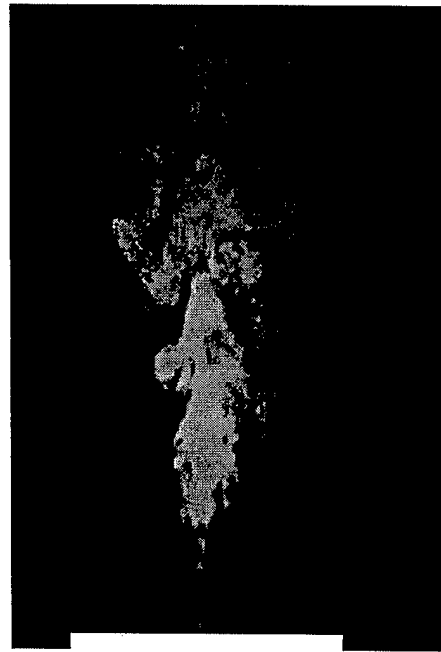**Figure 11 Cross section of fabricated microjet.**

Figure 12   Smoke visualization of operational microjet.

Figure 12 is a smoke visualization photograph of the jet where the smoke is injected radially near the orifice edge. The field of view measures 89 mm in the streamwise (x) direction (x/d=500). The jet appears to become turbulent at or near the orifice, and spreads almost linearly with streamwise distance. Large coherent vortical structures are apparent in the far field of the jet. The Reynolds number of the jet based on the centerline velocity and its width at x/D = 15 is approximately 1400, with a jet velocity in excess of 15 m/s.

Individual jet control of microjet array elements can be achieved in a variety of ways. One method which we have used is that of a metallized flexible polyimide diaphragm. The metal electrodes on the diaphragm are patterned so that voltage can be individually applied to the region over each actuator cavity. A key feature of this design is that the diaphragm can be vibrated using either an external conventional transducer to drive all array elements in parallel or a sinusoidal drive voltage applied to the flexible diaphragm of individual array elements. Driving the membrane in either fashion results in cavity pressure variations and a jet flow through the orifice. An individual jet is modulated by either reducing the amplitude of the drive voltage of an individual array element (for electrostatic drive) or by electrostatically modulating the diaphragm vibration amplitude for that element (for piezoelectric drive).

In order to more fully realize the possibilities of silicon-based synthetic jets, it is necessary to etch structures which are much deeper and with higher aspect ratio into the silicon in order to better control the jets and to increase the amplitude and momentum of the jets. This can be accomplished with the new ICP plasma etcher obtained in part with the resources of this grant, and this work is currently underway.

References

C. Camperi-Ginestet, Y.W. Kim, N.M. Jokerst, M.G. Allen, M.A. Brooke, "Vertical Electrical Interconnection of Compound Semiconductor Thin-Film Devices to Underlying Silicon Circuitry," *IEEE Photonics Technology Letters*, vol. 4, no. 9, pp 1003-1006, September 1992.

Carpenter, B. N. and Pearlstein, A. J. (1996) "Simulation of Extraction of Velocity from Passive Scalar Data in a Two-Dimensional Diverging Channel Flow," *Physics of Fluids*, 8, 2447-2459.

H. Cat., J. Eble, D. Wills, V. De, M. Brooke, N. Jokerst, "Low Power Opportunities for a SIMD VLSI Architecture Incorporating Integrated Optoelectronic Devices," GOMAC'96, pp. 59-62, FL, Mar. 1996.

Fourguette, D. C., Dimotakis, P. E., Ching, W. K. (1995) "Index-of-refraction Imaging and Aero-Optics Effects in a Fully-Developed Axisymmetric Turbulent Jet," *AIAA Paper 95-1980.*

Glezer, A., Kadioglu, Z. and Pearlstein, A. J. (1989) "Development of an Extended Proper Orthogonal Decomposition and its Applications to a Time Periodically Forced Plane Mixing Layer," *Physics of Fluids A*, 1, pp.1363-1373.

Jacobson, S. A. (1995) "An Experimental Investigation Towards the Active Control of Turbulent Boundary Layers," Ph.D. Thesis, Stanford University.

Lumley, J. L. (1967) "The Structure of Inhomogeneous Turbulent Flows," in *Atmospheric Turbulence and Radio Wave Propagation*, edited by A.M.Yaglom and V.I. Tatarskii, Nauka, Moskow.

Lumley, J. L. (1981) "Coherent Structures in Turbulence," in *Transition to Turbulence* edited by R.E.Meyer, Academic Press, New York, pp.215-242.

Pearlstein, A. J. and Carpenter, B. N. (1995) "On the Determination of Solenoidal or Compressible Velocity Fields from Measurements of Passive or Reactive Scalars," *Physics of Fluids*, 7, 754-763.

Wiltse, J. M. and Glezer, A. (1993) "Manipulation of Free Shear Flows Using Piezoelectric Actuators," *Journal of Fluid Mechanics*, 249, 261-285.

Coe, D.J.; Allen, M.G.; Smith, B.L.; Glezer, A. (1995) "Addressable micromachined jet arrays", 8th International Conference on Solid-State Sensors and Actuators and Eurosensors IX, Digest of Technical Papers, p.329-32 vol.2

JAN 1 6 1998

January 9, 1998

In reply refer to: **E-21-Z26**

Dr. James M. McMichael
AFOSR/NA
110 Duncan Avenue
Suite B115
Bolling AFB, DC 20332-8080

Subject: **Final Technical Report**
Project Director: M.G. Allen/A. Glezer/N.M. Jokerst
Telephone No.: (404)894-5251
Contract No.: **F49620-95-1-0181**
Prime No.: **N/A**
"EQUIP FOR NEURAL NETWORK DETERMINATION OF OPTICAL PHASE CORRECTION USING..."
Period Covered: 950301 through 970731

The subject report is forwarded in conformance with the contract/grant specifications.

Should you have any questions or comments regarding this report(s), please contract the Project Director or the undersigned at 404-894-4764.

/tw

Sincerely,

Wanda W. Simon
Reports Coordinator

Distribution:
Addressee: 1 copy